Analysis and Multidisciplinary Optimization of Internal Coolant Networks in Turbine Blades

Thomas J. Martin[*]

Pratt and Whitney Engine Company, East Hartford, Connecticut 06108

and

George S. Dulikravich[†]

University of Texas at Arlington, Arlington, Texas 76019

The theoretical methodology, conceptual demonstration, and validation of a fully automated computer program for the inverse design and optimization of internal convectively cooled three-dimensional axial gas turbine blades is presented. A parametric computer model of the three-dimensional internal cooling network was developed, including the automatic generation of computational grids. A boundary element computer program was written to solve the steady-state, nonlinear heat conduction equation inside the internally cooled and thermal barrier coated turbine blade. A finite element algorithm was written to model an arbitrary network of internal coolant passages for the calculation of the internal pressure losses, flow rates, effects of centrifugal pumping, heating of the coolant fluid, and heat transfer coefficients from the thermal model of the solid to the coolant fluid. The heat conduction and internal flow analyses were strongly and iteratively coupled to account for the heat balance between the blade and the coolant fluid. A system of evolutionary optimization algorithms was used to modify the internal cooling configuration and internal heat transfer enhancements (boundary-layer trip strips and pedestals) to achieve the objectives of increased cooling effectiveness and greater durability against oxidation, corrosion, and creep. The computer-automated design and optimization system was demonstrated on the second high-pressure turbine blade row of the Pratt and Whitney F100 engine. The internal cooling optimization on the product definition of this blade yielded a 5% increase in average cooling effectiveness, with only a marginal increase in coolant flow rate, in addition to having the same corrosion life and a doubling of the creep life.

Nomenclature

A	=	cross-sectional area of a coolant passage
C_D	=	coolant flow discharge coefficient
C_f	=	skin-friction coefficient
D_h	=	hydraulic diameter of a coolant passage
E	=	Young's modulus of elasticity
e_S	=	internal blade strut or rib fillet radius
e^+	=	roughness Reynolds number
$F(V)$	=	optimization objective function
f	=	friction factor
G_c	=	coolant mass flow rate
$G(V)$	=	optimization constraint function
H	=	coolant passage height from pressure to suction side
h_C	=	heat transfer coefficient on internal (coolant passage) surfaces
h_G	=	heat transfer coefficient on external (hot gas) surface
h_r	=	rothalpy
k	=	thermal conductivity of the blade material
M	=	local flow Mach number
N_{FE}	=	number of fluid elements
N_{FN}	=	number of fluid nodes
Nu	=	local Nusselt number
Pr	=	Prandtl number
ΔP_{ped}	=	pressure drop through a bank of pedestals
ΔP_{TRN}	=	pressure loss in a U bend
P_s	=	static pressure in coolant fluid system
P_t	=	total pressure in coolant fluid system
p	=	internal turbulator (boundary-layer trip strip) pitch
Q_c	=	heat flux through internal coolant passage surface
Q_G	=	heat flux from hot gas on external blade surface
Re	=	Reynolds number
R_K	=	coolant pressure loss coefficient in a U bend
S	=	surface area
St	=	Stanton number
s	=	blade cross section (local airfoil) contour coordinate
T	=	temperature
T_{aw}	=	adiabatic wall temperature
T_{film}	=	coolant film temperature
T_G	=	temperature of hot gas
T_{max}	=	maximum temperature
$T_{t,c}$	=	bulk total temperature of coolant
$T_{t,inlet}$	=	turbine inlet total temperature
t_m	=	thickness of blade wall
t_S	=	internal strut thickness
t_0	=	thickness of thermal barrier coating
V	=	set of optimization design variables
v	=	flow velocity of coolant fluid
W	=	coolant passage width from leading to trailing sides
x_S	=	coordinate of internal strut centerline intersection with turbine surface shape
α	=	turbulator rib (boundary layer trip strip) skew angle
Γ	=	boundary of computational domain
γ	=	ratio of specific heats of an ideal gas
ε	=	coolant passage wall roughness, trip strip or turbulator height
$\dot{\varepsilon}_C$	=	primary creep rate (strain rate)
η_f	=	coolant film effectiveness
θ_{irb}	=	in-plane angle of impingement rib inside the blade
θ_S	=	die pull angle, rib or strut angle clockwise off y axis

(partial right-margin nomenclature, cut off)

κ

μ

ρ

σ_r

ϕ

Ω

(right column, partially cut off)

V

in e
mei
mei
can
For
can
cool
ing
thic
losse
First
the c
vecti
terna

Ex
temp
layer
speci
showe
backs
comp
reduc
inlet t
enviro
tion of
when
holes.

This
multid
blades.
tem ca
that im
and/or
so that
The MI
within t
tools tha

II. Pa

A par
thermal
compute
gram (Be
robust ge
to pass i
cal analy
program
batch-pro
rithm. Th
two-dime
tended to
many of t
panies su

With th
of optimi
to represe
vane. The
coolant pa
passage w

κ = turbulent kinetic energy
μ = fluid viscosity coefficient
ρ = density
σ_r = centrifugal stress
ϕ = cooling effectiveness or convection efficiency of the coolant
Ω = rotor angular speed of rotation

I. Introduction

WITH presently available materials such as nickel-based alloys,[1] turbine blades cannot withstand metal temperatures in excess of approximately 1300 K. Internal heat transfer enhancements, such as trip strips or boundary-layer turbulators, impingement cooling, banks of pedestals, and miniature heat exchangers can provide significant enhancements of convection heat transfer. For example, when needed in the initial turbine stages, cooling air can be made to impinge on the leading- and trailing-edge internal cooling passage surfaces to enhance convection. Impingement cooling schemes demand large leading- and trailing-edge diameters and thicker blades that often cause substantially increased aerodynamic losses. Other complex heat exchangers have two major drawbacks. First, they induce early transition to turbulence and greatly increase the coolant passage friction, while moderately increasing the convective heat transfer. Second, the manufacture of such complex internal configurations requires special machining processes.

External (film) cooling techniques allow even greater inlet gas temperatures, up to 1800 K. Film cooling can produce a protective layer of cool air on the surface of the blade, and it can be targeted on specific areas of the blade that absorb the most heat, for example, shower head cooling at the leading edges. This has several drawbacks. High-pressure cooling air must be bled from high-pressure compressor stages, which results in external pressure losses due to a reduction in the boundary-layer momentum. The efforts to push the inlet turbine gas temperatures even higher are also constrained by environmental regulatory factors. The main problem is the production of NO_x that starts occurring at high gas temperatures, especially when mixing it with coolant ejected through the blade surface film holes.

This paper presents a portion of a dissertation on the topic of multidisciplinary design and optimization (MDO) of cooled turbine blades.[2] It has been demonstrated[2,3] that a computer-automated system can generate realistic internally cooled turbine blade designs that improve the efficiency and output of gas-turbine components and/or make the individual cooled blades and vanes more durable so that engine operational, repair, and warranty costs are reduced. The MDO program was developed to demonstrate such a system within the framework of design methodologies and computational tools that are currently used in the turbomachinery industry.

II. Parametric Model of the Internal Cooling Network

A parametric model for three-dimensional internally cooled and thermal barrier coated turbine blades and vanes was developed for computer-automated design and optimization. A FORTRAN program (BetaCore) was written with the intent of providing rapid and robust geometry generation of realistic turbine blades and vanes and to pass information between the parametric model and the numerical analysis programs automatically, without user intervention. The program was developed so that it could be executed in a parallel batch-processing environment by a numerical optimization algorithm. The parametric model was initially constructed to represent two-dimensional cooled turbine airfoils.[4,5] It has since been extended to three-dimensional turbine blades and vanes, including many of the complex features used by turbomachinery engine companies such as turns, impingement holes, pedestals, etc.

With the execution of this geometry generation program, a set of optimization design variables (the parametric model) was used to represent a virtual (electronic) prototype of the turbine blade or vane. The optimization design variable set controlled the internal coolant passage configuration, thickness variation of the coolant passage wall, positions and thicknesses of the internal ribs, die pull angles of the ribs, internal turbulator heights, turbulator pitches, turbulator skew angles, internal impingement hole diameters, impingement hole pitches, trailing-edge slot feature lengths, internal pedestal diameter, pedestal spacings, coolant supply pressures, and turbine inlet temperature. The program produced a boundary element (BEM) surface mesh that was imported directly into a heat conduction analysis code in the blade material. The mesh was prepared by BetaCore so that the boundary conditions could be automatically mapped between the interfacial surfaces. This information was transferred between the various design, optimization, and numerical analysis tools without user intervention. A constrained hybrid optimization algorithm[6] controlled the overall operation of the system and guided the multidisciplinary internal turbine cooling design process toward the objectives of cooling effectiveness and turbine blade durability. Design variable sets that generated an infeasible or impossible geometry were restored to a feasible shape automatically, using a constraint subminimization.

III. Hybrid Evolutionary Optimization Program

A constrained evolutionary hybrid optimization[6] computer program was developed in the FORTRAN programming language and incorporated into the computer-automated design and optimization system for internal turbine blade cooling. This algorithm creates sequential populations of feasible design variable sets V that evolve with each new optimization cycle by minimizing the objective function $F(V)$ associated with a finite number N_{pop} of design population members. Only feasible sets of design variables from the current optimization cycle are saved into the population matrix, $P\{V_1, V_2, \ldots, V_{N\,pop}\}$. These design variables are subject to a finite number of constraints, including lower and upper bounds on the design variables, V_{min} and V_{max}, respectively, and a finite number of inequality and equality constraint functions, $G_m(V) < 0$ and $H_n(V) = 0$.

This new hybrid optimization program incorporated four of the most popular optimization algorithms: the Davidon–Fletcher–Powell gradient search, a genetic algorithm, the modified Nelder–Mead simplex method, and simulated annealing. Each technique provides a unique approach to optimization with varying degrees of convergence, reliability, and robustness at different cycles during the iterative optimization procedure. A set of rules and switching criterion were coded into the program to switch back and forth between the different algorithms as the iterative minimization process proceeded.

IV. Inverse Design of Turbine Blades for Structural Integrity and Creep Life

Given a fixed external blade shape, inverse shape design was used to meet the creep life of the blade and the centrifugal stress limit. In cooled turbine blade design, the forward design process begins with the generation of an internal cooling scheme, and then the stresses or temperatures are calculated later using some analysis tool. Inverse design works in the opposite direction. That is, with knowledge of the temperature or stress, it is possible to determine an unknown geometry that is compatible with this stress and temperature data. Inverse design is possible only if some additional information, albeit approximate and a priori, is available in addition to what would be boundary conditions of a well-posed (forward) problem. In the internally cooled turbine blade case, the designer must know what stresses are to be allowed in the blade. It is well understood that the stress at the blade root may not exceed the yield stress σ_y. However, blades are also designed to have a certain life span that is severely limited by temperature-dependent creep. Therefore, the designer also needs to know something about the radial variation of the blade temperature so that the internal cooling scheme can be designed to maintain a certain average creep life requirement. That is, the average creep life of the blade is specified first. Then, after computing the radial variation of the centrifugal stress limit from this requirement, the thickness of the coolant passage wall is determined not to exceed the centrifugal stress limit.

Given the nonuniform combustor exit flow profile and the highly three-dimensional nature of the aerodynamics, the hottest gases in

the turbine tend to migrate to the midspan radius, whereas the centrifugal stresses in the blade are the highest at the root of the blade and decrease radially. The combined three-dimensional temperature and stress environment provides that the worst creep is experienced at some critical span location between the root and the tip. Thus, a radial gas temperature profile $T_G(r)$ from a computational fluid dynamics (CFD) calculation was used to approximate a radial variation of the blade's metal temperature $T_m(r)$. This required some approximate knowledge of the average heat transfer coefficients precalculated or assumed on the blade's external surface, h_G, and on the internal coolant passage surfaces, h_C. A nominal blade wall thickness t_m, a nominal thermal barrier coating thickness t_0, and a bulk coolant temperature T_C were also needed. The following analytic solution for one-dimensional heat transfer can be used to calculate spanwise variation of wall temperature:

$$T_m(r) = \frac{h_G T_G (1 + h_C t_m/k_m) + h_C T_C (1 + h_G t_0/k_0)}{h_G(1 + h_C t_m/k_m) + h_C(1 + h_G t_0/k_0)} \quad (1)$$

where k_m and k_0 are the coefficients of thermal conductivity of the metal and coating, respectively. It is understood that this is a severe approximation that does not model the multidimensionality of the problem because the real geometry and temperatures are not known before this equation is used. The internal heat transfer coefficients h_C and bulk coolant temperatures T_C did not have radial or passage-to-passage variations either, and so only average values were used. The temperature dependence of thermal conductivity was also ignored. The thermal mixing within the turbine blade cascade, as well as the migration of hot gases, is a highly three-dimensional fluid flow phenomenon, and, thus, it was not reflected by Eq. (1) either.

With this approximate blade surface temperature variation $T_m(r)$ and a given average creep life of the blade $\dot{\varepsilon}_C$, the radial variation of the allowable centrifugal stress in the blade metal was estimated using the Larson–Miller relation where the mean creep life was quantified by a function of stress, temperature and time.[7] The following equation was experimentally derived to relate creep rate to temperature and stress[8]:

$$\log(\dot{\varepsilon}_C) = C_0 + C_1/T + C_2 \log[\sinh(C_S \sigma/E)] \quad (2)$$

In this equation, σ is the stress and C_0, C_1, C_2, and C_S are constants. This equation was solved for σ [now called $\sigma_{r,\max}$, given $T_m(r)$ for T] from the critical span (radial location of the blade that has the highest metal temperature) out to the blade tip. For the rest of the blade, the maximum allowable stress $\sigma_{r,\max}$ was linearly increased from the stress at the critical span to the tensile yield stress σ_Y at the root.

An iterative root-finding inverse design procedure was used to determine the radial variation of the coolant passage wall and internal rib thicknesses. In this iterative procedure, the two-dimensional turbine blade sections were generated from the tip to the root, whereas the nominal wall thicknesses were increased when the calculated centrifugal stress exceeded the specified allowable stress from Eq. (2). The resulting parametric blade representation was implicitly able to maintain the centrifugal loads, as well as meet the creep life constraint (assuming some margin of errors caused by three dimensionality, hot gas migration, thermal mixing, uncertainty in geometry and operating conditions, etc). In the design of this turbine blade, a ±5–10% margin of error in coolant flow rate was accounted for with a 5% margin of error in metal temperature T_m.

V. Cooling Effectiveness

When it is assumed that the external (hot gas) aerothermodynamics is fixed, and there is no film cooling, the optimization objective function takes the form of a thermal-only optimization function. For internal convective cooling schemes, an optimization objective can be mathematically formulated as the maximization of the cooling effectiveness or convective efficiency:

$$F(V) = \phi = \int_{\Gamma_E} \frac{T_G - T}{T_G - T_{t,c}} \, d\Gamma \quad (3a)$$

In this equation, $T_{t,c}$ is the coolant total temperature at the inlet to the coolant passages, T is the metal temperature, and Γ_E indicates the

external surface of the turbine blade. Maximization of this objective function drives the temperature of the turbine blade or vane toward the coolant temperature, thus improving its durability. However, this function has no penalizing effect to compensate for the increased coolant flow rates possibly worsening the engine cycle efficiency and for increased supply pressure causing greater leakage losses. On the other hand, if the coolant supply temperature $T_{t,c}$ is a degree of freedom, the process of minimizing the cooling effectiveness may drive the coolant temperature higher because enhancements to the internal heat transfer coefficients are correlated with higher pressure losses. Therefore, the bleed air must be taken from higher compressor stages where the air temperatures are higher because of compression and because these stages are in closer proximity to the burner. The use of the convective efficiency objective function has an element of risk and so should be penalized by the supply coolant pressure and/or coolant flow rate. For example, one such penalized objective function that could be minimized for a coolant effectiveness optimization is

$$F(V) = G_c/\phi P_{t,c} \quad (3b)$$

In this equation, G_c is the internal coolant flow rate, ϕ is the convective efficiency, and $P_{t,c}$ is the total pressure at the inlet to the coolant passages.

VI. Thermal Integrity and Durability Against Corrosion

The material integrity and blade durability against oxidation and corrosion were maintained with a constraint function by ensuring that the maximum temperature in the blade material did not exceed its thermal or corrosion life limit $\bar{T}_{\max}$. Thus, the optimization constraint function for thermal integrity was formulated as follows:

$$G(V) = T_{\max}/\bar{T}_{\max} - 1 <= 0 \quad (4)$$

Internally cooled turbine blade configurations were said to be feasible whenever this condition was satisfied, as were the other constraints such as aerodynamic loading, structural integrity, and the coolant air bleed pressure being high enough to drive the internal coolant flow.

VII. External Aerothermodynamics

A viscous three-dimensional CFD turbomachinery analysis code (SWIFT/RVC3D) has been used and validated for pressure field prediction[9,10] and for a transonic turbine airfoil cascade tested by Giel et al.[11] The external hot gas heat transfer coefficient h_G was determined from the CFD-computed heat flux given an arbitrary reference hot gas temperature T_G. The value of T_G was either the inlet total temperature $T_{t,\text{inlet}}$, which was either spanwise averaged or spanwise varying, or it was set to the adiabatic wall temperature T_{aw}, from a second CFD calculation. Heat transfer coefficients on the blade external surface were computed from the converged hot surface temperatures and fluxes and the corresponding turbine inlet total temperature $T_{t,\text{inlet}}$:

$$h_G = Q_G/(T - T_{t,\text{inlet}}) \quad (5)$$

When external film cooling was used, the adiabatic wall temperature was converted to a film temperature T_{film} via the adiabatic film effectiveness[1]:

$$\eta_f = \frac{T_{aw} - T_{\text{film}}}{T_{aw} - T_{t,c}} \quad (6)$$

where $T_{t,c}$ is the stagnation temperature of the film cooling air. The film cooling effectiveness η_f is derived from an empirical correlation to experimental data. Its local variation is a function of the film cooling air injection flow rate, total pressure, incidence angles, and the contour-following surface distance downstream of the film holes.

To obtain the variation of external convective heat transfer coefficient h_G the CFD analysis was executed with a constant wall temperature boundary condition. This CFD analysis required a turbulence

model with an accurate prediction of the location of boundary-layer transition to turbulence. A two-equation κ–ω model was used with a fine enough grid within the boundary layer to resolve the heat transfer (using $y^+ < 2$) accurately. For accurate heat transfer calculations, the CFD code was converged to a greater level of accuracy than one would normally need for reasonable pressure field accuracy.

VIII. Boundary Integral Equation for Heat Conduction

The nonlinear heat conduction equation was solved computationally with the BEM.[12] The BEM has been chosen for two reasons. First, the boundary-only nature of the BEM did not require grid generation within the cooled and thermal barrier coated turbine material. Second, the BEM system was easily differentiated with respect to the optimization design variables, thus allowing cheaper and more accurate calculations of the design sensitivity coefficients. Implicit differentiation for the design sensitivities ultimately resulted in a 3-time speed up in convergence to the minimum for two-dimensional thermal optimization problems and more than 10-time speed up for three-dimensional thermal optimization problems.[2]

The following partial differential equation governs the steady conduction of heat within an inhomogeneous solid blade made up of one or more materials having different temperature-dependent material properties.

$$\nabla \cdot (k_m \nabla T) = 0 \tag{7}$$

Multiple material subdomains were necessary for modeling turbine blades with thermal barrier coatings.

IX. Internal Coolant Network Analysis

The internally cooled turbine blade problem involves a complex internal coolant flow network with many branches. Methods for calculating flow rate and pressure losses in such a system are similar to methods for analyzing electrical networks, but it is highly nonlinear, and a large number of parameters have a significant effect on the energy conservation and flow losses. Much of the heat transfer is due to high heat transfer coefficients resulting from fully developed turbulence brought on or enhanced by turbulators, impingements, turns, and pedestals. Frictional shear forces cause most of the internal pressure losses, and these can be correlated to the passage length, wall roughness, and velocity with a nonlinear friction coefficient. Compressibility is another source of loss that does not have such a correlation, but is considered in the conservation laws. Also, inlet losses can have a significant influence on the total losses, especially for rotating passages. Asymmetry of the inflow resulting from a change in the flow direction into the passages produces an adverse pressure gradient that can result in local flow separation.[13] As the cooling fluid exits from the passages into the surrounding transonic gas flow, exit losses result from the disruption of the external boundary layer. Discharge coefficients are needed to determine the actual cooling flow rates and momentum flux through exits and film cooling holes. With the addition of complex heat exchangers, banks of pedestals, rows of skewed internal ribs or trip strips, 180-deg bends, internal impingements, and other heat transfer enhancements, the quasi-one-dimensional prediction of internal compressible flow losses and coolant fluid heating must be correlated with a great deal of empirical data over a broad range of operating conditions, configurations, and characteristics.

A quasi-one-dimensional compressible thermofluid flow network program (COOLNET) was written in FORTRAN to predict coolant flow rate G_c, total coolant pressures p_t, bulk coolant total temperatures $T_{t,c}$, and internal heat transfer coefficient distributions h_C, inside internally cooled turbine blades and vanes. It was written as a generalized finite element method (FEM) program for thermofluid elements and adapted into the computer-automated design system for optimization. The coolant passages were allowed to be an arbitrary network of one-dimensional fluid elements or tubes. The lengths, cross-sectional areas, perimeters, wall roughness, heat transfer enhancements, etc., were specified uniquely for each fluid element. This locally one-dimensional geometric information was mapped automatically from the three-dimensional parametric model to the input deck of the COOLNET algorithm.

The FEM solved the thermofluid network problem for a specified inlet relative total pressures, inlet relative total temperatures, and exit static pressures. The equations were solved by a Picard iteration strategy due to the nonlinearity of the pressure loss functions. The stability and convergence of the solution technique depended on the accuracy of the initial guess for the local mass flow rates. Under-relaxation was used when updating the flow rates G_m in each fluid element. The initial guess to the internal coolant flow rates was set up using local area-weighted flow splitting at each nodal junction connecting three or more coolant fluid elements.

A. Internal Total Pressure and Flow Balance

The relative total pressure drop ΔP_t across each element that rotates with angular speed Ω is governed by the momentum conservation equation. Pressure changes due to friction ΔP_f, acceleration of the flow by heating ΔP_a, and centrifugal pumping ΔP_c are summed up as the total pressure change[14,15] between nodes 1 and 2:

$$A_2 P_{t,2} - A_1 P_{t,1} = S \Delta P_f + A(\Delta P_a + \Delta P_c) \tag{8}$$

Here, A is the cross-sectional area and $S = P \times L$ is the surface area (perimeter times length) of the element. The pressure loss due to friction ΔP_f is proportional to the dynamic pressure. The pressure change due to centrifugal pumping ΔP_c was derived from the momentum equation in cylindrical coordinates. The flow accelerates when heat is added to the fluid, so that the pressure change due to heating is included with the addition of the term ΔP_c. Hence, the three kinds of total pressure change are given, as follows:

$$\Delta P_f = -C_f \tfrac{1}{2} \rho v^2 \tag{9}$$

$$\Delta P_a = (\gamma/2) M^2 [(T_{t2} - T_{t1})/T_{t1}] P_t \tag{10}$$

$$\Delta P_c = \rho R \Omega^2 (R_2 - R_1) \tag{11}$$

where ρ is the coolant density, v is the local coolant speed, M is the local coolant Mach number, T_{t1} is the relative total temperature of the coolant, R is the radius from the engine centerline, and P_t is the relative total pressure of the coolant.

When the element was an exit path, the total pressure was related to the static (dump) pressure. To model these elements, the friction coefficient was set to unity, $C_f = 1.0$. A discharge coefficient C_D was also needed to determine the actual film cooling flow rates. C_D was defined as the ratio of the actual mass flow rate G to the ideal mass flow rate. The ideal mass flow rate was calculated by assuming an isentropic one-dimensional expansion from the total pressure P_t to the static pressure P_s:

$$C_D = G \left/ P_t \left(\frac{P_s}{P_t}\right)^{(\gamma+1)/2\gamma} A \sqrt{\frac{2\gamma}{(\gamma-1)RT_t}\left[\left(\frac{P_t}{P_s}\right)^{(\gamma-1)/\gamma} - 1\right]}\right. \tag{12}$$

Equation (10) was used to calculate the mass flow rates during the iterative solution procedure. Discharge coefficients were dependent on local coolant passage geometry, as well as internal and external flow conditions.[13,16]

The mass flow through the element, $G = \rho A v$, is an unknown in this system. Continuity gives equilibrium conditions at the nodes of the fluid network. G_m is positive entering the node and negative leaving the node. The summation is over each mth element attached to the node:

$$\sum_m G_m = 0 \tag{13}$$

The N_{FE} elemental pressure balance equations were cast into a local FEM matrix form:

$$\begin{bmatrix} \dfrac{2A_1}{C_f v} - \dfrac{2A_2}{C_f v} - 1 \end{bmatrix} \begin{Bmatrix} P_{t,1} \\ P_{t,2} \\ G_{12} \end{Bmatrix} = -\dfrac{2A}{C_f v}[\Delta P_a \quad \Delta P_c] \quad (14)$$

where $G_{12} = -G_{21}$. The N_{FE} local FEM pressure balance equations were combined with the N_{FN} nodal equilibrium equations to form a global FEM system. Pressure boundary conditions were applied at the inlet and exit (source and sink) nodes of the network. It was standard practice to apply total pressures $P_{t,i}$ at all inlet nodes and static pressures $P_{s,j}$ at all exit nodes, where $I = 1, \ldots, N_{in}$ and $j = 1, \ldots, N_{ex}$. The fluid network was allowed to have an arbitrary number of inlet nodes N_{in} and exit nodes N_{ex}. The equilibrium equations were written only at the internal nodes because they are not applicable at inlet and exit nodes. If the network had N_{in} inlets and N_{ex} exits, the global finite element system would have an equal number, $(N_{FE} + N_{FN} - N_{in} - N_{ex})$, of equations and unknowns that were solved for the unknown total pressures at each internal node and local coolant flow rates in all elements.

B. Internal Enthalpy Conservation

The one-dimensional enthalpy conservation equation was solved to calculate the bulk coolant total temperatures $T_{t,c}$ of the convecting and rotating coolant fluid. Convective heat transfer through the walls of the coolant flow passage Q_c accounted for heat addition. The energy equation for the cooling air was expressed in local finite element matrix form in terms of total rothalpy H_r:

$$\begin{bmatrix} G & -G \\ -G & G \end{bmatrix} \begin{Bmatrix} H_{r,1} \\ H_{r,2} \end{Bmatrix} = \begin{Bmatrix} -Q_c S \\ Q_c S \end{Bmatrix} \quad (15)$$

where S is the surface area exposed to the coolant fluid. The total rothalpy[1] at each node is defined by

$$H_r = C_p T_C + \tfrac{1}{2}v^2 - \tfrac{1}{2}r\Omega^2 \quad (16)$$

where C_p is the specific heat, T_C is the bulk coolant static temperature, r is the radius from the engine centerline, and Ω is the rotor speed. The heat flux Q_c was obtained by a three-dimensional BEM analysis of the heat conduction in the turbine blade. The system of equations (13) was generated for each fluid element and assembled into a global system using the FEM. The solution of this system required that the bulk total temperature of the coolant $T_{t,c}$ be specified at all inlet paths.

The global pressure and rothalpy systems resulted in coefficient matrices that needed to be inverted at every iteration of the COOLNET algorithm. The pressure system was slightly ill conditioned when large complex internal networks were solved, and so singular value decomposition[17] was used to invert that matrix. The result of these matrix inversions were values of the total pressure at every internal node, the mass flow rate through every element, and the rothalpy at every internal and exit node.

C. Forced Convection Correlations for Friction Factors

In an effort to enhance heat transfer, modern cooling designs utilize turbulators such as trip strips or transverse ribs to increase the internal heat transfer coefficients. They induce early transition to turbulence and greatly increase the channel friction and pressure losses, while moderately increasing the convective heat transfer.[18] A large number of heat transfer and pressure loss correlations appear in the open literature and in textbooks. Several of those that pertain to internal cooling of turbine blades have been adapted into this research and used to predict pressure losses and heat transfer coefficients by COOLNET.

To generate heat transfer coefficients, the Reynolds analogy was adequate only for uniform fully rough walls, but more rigorous correlations were needed to predict the friction and heat transfer characteristics of passages with trip strips or turbulators. Webb[19] categorized many possible roughness geometries that are used in commercial applications into three basic roughness families: uniform, repeated ribs, and grooves. The key dimensionless variables are

the roughness ratio (ε/D_h), roughness spacing (p/ε), the rib width $(\varepsilon_w/\varepsilon)$, and the shape of the roughness element. The "friction similarity law" was developed by Schlichting[20] for closely packed sand grain (uniform) roughness. The velocity profile, based on the law of the wall depends on the roughness Reynolds number e^+ and is obtained by integrating the velocity profile over the flow area:

$$\sqrt{8/f} = -2.5\,\ell n(2\varepsilon/D_h) - 3.75 + B(e^+)$$

$$e^+ = (\varepsilon/D_h)Re_D\sqrt{f/8} \quad (17)$$

Correlations have shown that the friction factor approaches the smooth tube value in the laminar regime. In the turbulent regime, the smaller ε/D_h values drift above the smooth tube line at higher Reynolds numbers and attain an asymptotic constant value that is termed the fully rough condition. Dipprey and Sabersky[21] developed a rational correlation based on the heat momentum transfer analogy for rough surfaces, and it is applicable to any geometrically similar roughness. The correlating function is obtained by integrating the momentum and energy equations over the boundary-layer thickness.

The Stanton number is now a function of the friction factor, the Prandtl number Pr, and the functions $G(e^+)$ and $B(e^+)$:

$$St = \frac{C_f/2}{1 + \sqrt{C_f/2}[G(e^+)Pr^\varphi - B(e^+)]} \quad (18)$$

The Stanton number, $St = h_C/\rho C_p v$, and the friction factor, $4C_f = f = 8\tau_w/\rho w^2$, were based on the properties of the bulk cooling fluid. The exponent φ is 0.44 for sand grain and 0.57 for transverse ribs. The $G(e^+)$ and $B(e^+)$ are different for the different roughness families. Webb[19] applied the model to geometrically similar transverse rib roughness where $p/\varepsilon = 10$, 20, and 40. The heat transfer similarity law correlates with the experimental data through a range of roughness ratios between 0.01 and 0.045. Correlations for the combined effects of rib angle of attack and coolant passage aspect ratio on the distributions of local heat transfer coefficient were provided by Han and Park,[22] which involved developing flow in short rectangular channels with a pair of opposite rib-roughened walls.

Most internal cooling schemes have passages that cause the coolant fluid to undergo sharp turns so that it can flow radially outward toward the tip of the blade and radially inward toward the root several times. This is known as multipass or serpentine cooling scheme. The pressure losses in 180-deg bends, ΔP_{TRN}, were assumed to be proportional to the dynamic pressure[23]:

$$\Delta P_{TRN} = \tfrac{1}{2}\rho v^2 R_K, \qquad R_K = 0.4/(36.37 D_h)^{0.2} \quad (19)$$

where the hydraulic diameter D_h is in meters. Typically, the pressure loss factor R_K for bends of a serpentine inside internally cooled turbine blades is about 2.5–3.5.

Trailing-edge coolant flow passages often involve multiple rows of heat exchanging pedestals. The pressure drop, ΔP_{ped}, for flow of gases through a bank of pedestals having 10 or more rows was expressed as follows[24]:

$$\Delta P_{ped} = \left(2f'G_{max}^2 N_{bank}/v^2\right)(\mu_w/\mu_{cool})^{0.14} \quad (20)$$

G_{max} is the coolant mass flow rate at minimum flow area (kilograms per meters squared per second) and N_{bank} is the number of transverse rows. Jakob (see Ref. 24) gave the empirical friction factor for staggered pedestal arrangements:

$$f' = \left\{0.25 + \frac{0.118}{[(S_n - D)/D]^{1.08}}\right\} Re_{max}^{-0.16} \quad (21)$$

The heat transfer characteristics in a rotating serpentine coolant flow passage are very complex and three dimensional, being affected by Coriolis forces and centrifugal forces combined with thermal buoyancy. Hot zones have a distinct effect on the heat transfer rate because higher temperatures produce greater buoyancy forces and enhanced heat transfer. Secondary flows are induced by the Coriolis

force, making the heat transfer coefficients in the radially outward passages diminish on the leading surfaces and increase on the trailing surfaces, with an increase in rotational speed. The trend is reversed in the radially inward passage. To account for the rotating serpentine flow, the ratio of rotating to nonrotating heat transfer coefficients, Nu_r/Nu, was adjusted.[22,25]

X. Coupled Heat Conduction and Internal Thermofluid Dynamics

The external aerothermodynamics, the heat conduction in the cooled airfoil, and the heat pickup by the internal coolant flow network were strongly coupled together and iterated until a heat balance was realized such that the temperature everywhere in the model did not change by more than 0.5 K during the conjugate iterative procedure. Internal heat transfer coefficients and bulk coolant temperatures were determined with an internal coolant flow network solver (COOLNET) and applied to the internal boundary elements. The coolant heat transfer coefficients h_C and bulk coolant temperatures $T_{t,c}$ were allowed to vary radially, around turns, from passage to passage, and differently on the pressure, suction, and rib sides. The external aerothermodynamics was solved for by the CFD algorithm (SWIFT). The BEM analysis used the external surface heat transfer coefficients h_G, adiabatic wall or film temperatures T_{aw} or T_{film}, internal heat transfer coefficients h_C, and bulk coolant temperatures $T_{t,c}$, specified to the internal boundary elements exposed. The BEM heat conduction analysis then predicted a temperature field inside the blade material, T, heat fluxes on the coolant passage walls, Q_c, and a temperature variation on the external blade surface, T, that were different from the initial guess. For stability, the surface area-averaged internal wall temperature $T_{w,av}$ was used instead of the heat fluxes Q_c applied to each fluid element:

$$Q_c = h_C(T_{w,av} - T_{t,c}) \tag{22}$$

In the next iteration, the new external wall temperature variation T was applied as a thermal boundary condition again to the CFD code. Because of the coolant fluid heating, the COOLNET algorithm was executed iteratively with the BEM heat conduction code with new integrated heat fluxes Q_c applied to each internal fluid element. During each iteration, COOLNET predicted new internal heat transfer coefficients h_C and new bulk coolant temperatures $T_{t,c}$ that were different from the preceding iteration. These new boundary conditions h_C and $T_{t,c}$ were then applied to the BEM heat conduction analysis. This solution procedure continued until the integrated heat flux residuals converged to a reasonable tolerance. A flow chart of the multidisciplinary design, conjugate analysis, and optimization system for internal turbine airfoil cooling is given in Fig. 1.

XI. Validation of the Internal Coolant Network Flow Solver

The F100 family of military turbofan engines features a twin-spool, axial-flow design with a bypass ratio of 0.63. The F100-PW-100 engine powers the F-15 fighter with 105,000-N maximum takeoff thrust and a total airflow of 100 kg/s. The F100 engine has a three-stage fan driven by a two-stage low-pressure turbine. A two-stage high-pressure turbine drives the 10-stage high-pressure compressor. The overall fan and compressor ratio is 24.8. Several examples and optimization test cases will be demonstrated on the second blade of the high-pressure turbine because it does not have film cooling. Figure 2 illustrates a representative cross section of the F100 second turbine blade at the midspan. The parametric representation is shown with filled square symbols, and the actual geometry is shown without symbols. Figure 3 shows the boundary element mesh for the internal coolant passages where the external blade surface boundary elements were removed.

The thermofluid network flow solver was verified against data from a bench test of a stereolithography model. The second rotor blade of the Pratt and Whitney F100 engine was used for this purpose. This blade utilizes a three-pass serpentine design with two feed passages and ejection of the internal cooling air at the tip. The internal configuration is illustrated in Fig. 4, and the internal coolant network of fluid elements used by COOLNET is shown in Fig. 5.

The first up-pass and the down-pass were enhanced with boundary-layer trip strips (TRP, Fig. 5). The second up-pass had

Fig. 2 Comparison of actual and parametrically modeled sectional shapes of a second rotor blade of Pratt and Whitney F100 high-pressure turbine.

Fig. 1 Flow chart for the multidisciplinary design and optimization of internally cooled turbine airfoils.

Fig. 3 BEM of the internal coolant passages with the external airfoil surface elements removed.

Fig. 4 Cross section schematic of the Pratt and Whitney F100 second blade.

solution process, the inlet flow rates were assumed to have a Mach number of 0.1 in the feed paths (numbers 101 and 102) and area-based flow splitting was used to establish the remaining elemental flow rates. The results of the COOLNET computation are shown against the data from a Pratt and Whitney internal flow design code calibrated to the experimental pressure tap data in Figs. 6 and 7. Figures 6 and 7 show only data in the coolant flow passages above the platform. Thus, elements 11–14 are shown with boxes, elements 24–141 are shown with circles, and elements 31–36 are shown with diamonds. Because the actual values of the data are company sensitive, the axis labels have been removed.

Notice, though, that the trends and magnitudes are within acceptable limits. The main problem with the COOLNET algorithm was that it tended to predict a slightly higher flow rate (about 9–10%). This resulted in higher-pressure losses and lesser coolant fluid heating in all passages. The cause of this discrepancy is probably due to the discharge coefficients of the bleed holes in the Pratt and Whitney model being $C_D = 0.9$. In COOLNET, the BLD were modeled as smooth channels and nothing special was done at the inlet paths (numbers 101 and 102). Both COOLNET and the Pratt and Whitney internal flow design code predicted that the exit flow path (SQU in Fig. 5) that dumps the air into the tip pocket had reversed, and that

Fig. 5 COOLNET internal flow network model for the F100 second blade.

a bank of pedestals (PED, Fig. 5) that have been oriented in a certain pattern to avoid vibratory stresses. The pedestals were either circular or of an oblong circular shape. The coolant air is ejected at the tip of the blade and into the tip pocket. Several bleed holes (BLD, Fig. 5) across the leading-edge rib reduce the pressure losses around the first tip turn. Pressure taps were used to measure internal pressures, and a Pratt and Whitney proprietary flow model was calibrated to these data. The high-pressure turbine of the F100 test engine had a rotation rate of 13,467 rpm, corresponding to a takeoff condition.

COOLNET solved for the relative total pressures and total temperatures in about 40 iterations. At the starting point of the iterative

Fig. 6 Comparison of spanwise distribution of total pressures of internal coolant flow predicted by COOLNET vs Pratt and Whitney internal flow design code calibrated to experimental pressure tap data inside F100 second blade.
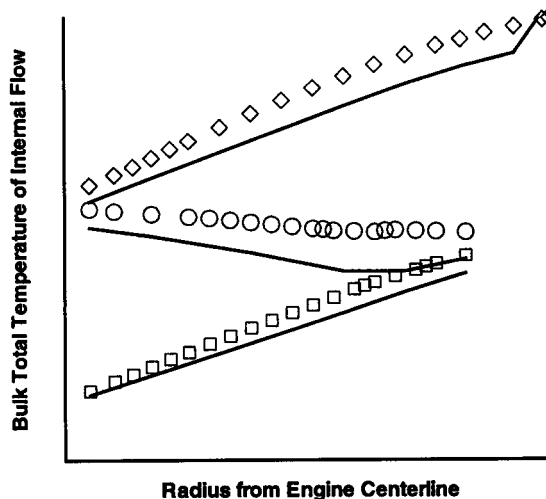
Fig. 7 Comparison of spanwise distribution of total temperatures of internal coolant flow predicted by COOLNET vs Pratt and Whitney internal flow design code calibrated to experimental pressure tap data inside F100 second blade.
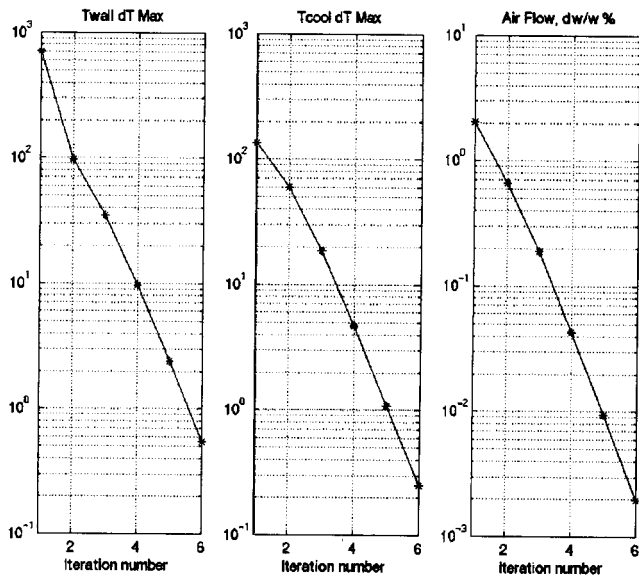
Fig. 8 Convergence rates for the maximum wall temperature, coolant total temperature, and coolant flow rate vs conjugate iteration number.

path 7000 was actually feeding the system. This effect appears in Fig. 7 in the upper right-hand corner.

XII. Validation of the Conjugate Heat Balance

Figure 8 illustrates the convergence rate for the maximum wall temperature, coolant total temperature, and coolant flow rate. Figure 8 shows the change in temperature or flow rate vs conjugate iteration number. Each conjugate iteration number is defined as one external CFD analysis with SWIFT using applied airfoil wall temperature variation, one thermal–fluid analysis of the internal coolant network with variable heat flux applied, and one BEM heat conduction analysis with applied external and internal heat transfer coefficients and internal bulk coolant temperatures. The convergence is rapid and stable because the nonlinearity is weak. After six iterations, the maximum change in wall temperature is approximately 0.25 K, the maximum change in cooling air temperature is approximately 0.125 K, and the change in total cooling airflow is approximately 0.002%.

XIII. Validation of the Aerothermofluid Analysis

A coupled aerothermofluid analysis was attempted on the second blade of the high-pressure turbine (HPT) of the Pratt and Whitney F100 engine to compare the computed wall temperatures with experimental pyrometry data taken during an engine test. The pyrometer was only able to view the trailing half of the suction side. Thermocouples were placed at the 10 and 50% spans of the external leading-edge surface, and thermocouple data were also gathered on the pressure sides at the 50% span. The uncertainty in the pyrometer measurements was +2.5/−5 K, and the uncertainty in the thermocouple measurements was ±6 K.

This aerothermofluid analysis coupled a three-dimensional NASA CFD code (SWIFT) with the κ–ω turbulence model for the rotor cascade, the nonlinear BEM for heat conduction analysis in the blade material, and the internal flow solver COOLNET. Figure 9 shows a comparison between the external wall temperature predicted by the iteratively coupled SWIFT, BEM, and COOLNET and the experimental data at the midspan (50%) of the second turbine blade. The contour following coordinate has its origin, $s = 0.0$, at the leading edge, and s is negative on the suction side. The aerothermofluid prediction is shown as the thick solid curve in Fig. 9. All calculations assumed a 10% freestream turbulence level, and rotational effects were not incorporated into the heat transfer coefficients predictions within COOLNET.

In Fig. 9a, two three-dimensional aerothermofluid calculations are shown at the midspan; one with no iterative heat balance but involving only a single CFD solution and a single COOLNET solution
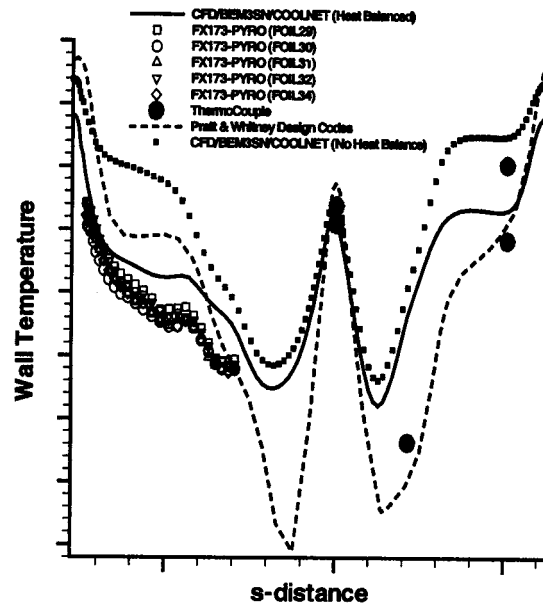

Fig. 9a Comparison of the conjugate predictions using the three-dimensional BEM codes, two-dimensional decoupled Pratt and Whitney design codes, and experimental pyrometer and thermocouple data from the second HPT blade of the Pratt and Whitney F100 engine.
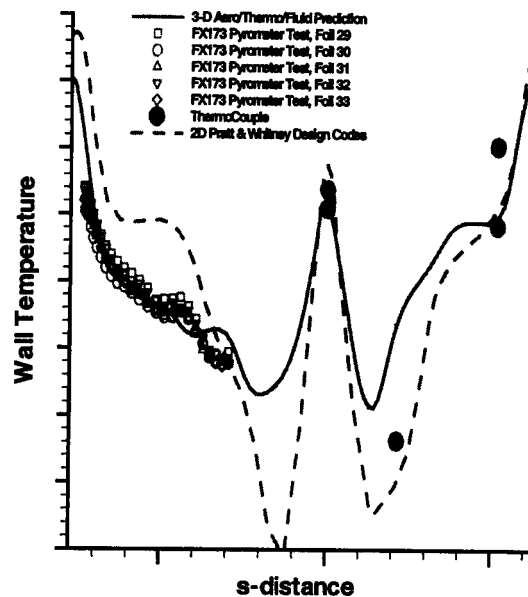

Fig. 9b Comparison of the three-dimension conjugate BEM predictions with centrifugal effects and experimental pyrometer and thermocouple data for surface temperature on the second HPT blade of the Pratt and Whitney F100 engine.

mapped to the BEM mesh (small square symbols) and one where the iterative heat balance between the BEM and COOLNET solvers was strongly coupled (solid line). These predictions are shown at the midspan vs the experimental pyrometer (open symbols) and thermocouple (filled circles) data. Notice that there was a significant heat-up of the coolant air as recognized by the 50 K temperature difference on the suction side between the heat-balanced and the non-heat-balanced solutions. The heat-balanced solution was obviously better. The disagreement between the prediction and the thermocouple data on the pressure was caused by CFD modeling of the boundary layer as fully turbulent rather than with a laminar-to-turbulent transition in the CFD prediction. Rotational effects were subsequently incorporated into the internal coolant flow model and used by COOLNET. The fully conjugate procedure and enhanced heat transfer introduced with rotational effects in the correlations

produced the best agreement between the CFD/BEM/COOLNET analysis and the pyrometer data, as shown by the solid line in Fig. 9b.

The three-dimensional aerothermal analysis of the blade was compared to an earlier two-dimensional Pratt and Whitney design code analysis of the same blade (see dashed line in Figs. 9a and 9b). The two-dimensional solution was developed by generating external heat transfer coefficient and adiabatic wall temperature variations with the two-dimensional STAN5[26] boundary-layer code at the midspan. The external heat transfer coefficients and adiabatic wall temperatures were applied to a two-dimensional finite differenced heat conduction program used as a design code at Pratt and Whitney's Turbine Module Center. In the STAN5 solution, the boundary layer was forced to transition from laminar to turbulent at the 10% chord location on both the pressure and suction sides. Note that this two-dimensional solution was produced after the pyrometry and thermocouple data were reduced. Thus, the fully coupled three-dimensional analysis has advantages of three dimensionality of the heat conduction, predictive capability in the regions of the airfol tip and platform, and fully automated coupling of the heat conduction and boundary condition programs, but at the expense of computational time.[27] Each fully coupled three-dimensional prediction of the temperature field using the aerothermofluid system required about 25 min of CPU time on a Sun Ultra-60 workstation (equivalent to less than 5 min on a 1.7-GHz Intel Xeo).

XIV. Cooling Effectiveness Optimization

The computer-automated design and optimization system was demonstrated on the second high-pressure turbine blade of the Pratt and Whitney F100 engine. The fully three-dimensional geometry of the coolant passages and internal heat transfer enhancements were optimized for maximum cooling effectiveness at a fixed coolant flow rate by minimizing Eq. (3a). The external aerodynamics and coolant supply pressure were held fixed during the optimization process, whereas parameters such as rib turbulator height, turbulator pitch, pedestal diameter, and internal rib positions were allowed to vary.

The optimization started from a design that was very similar to the actual product definition of the Pratt and Whitney F100 second turbine blade (see Figs. 2 and 3). The three-dimensional parametric model was used to generate the BEM for the three-dimensional turbine blade. The inverse shape design procedure was used to maintain creep life and structural integrity. The rib thicknesses and coolant wall thickness distribution were increased from the tip to the root to maintain the centrifugal load and creep life. With the generation of each new parametric design, the radial variations of wall rib thickness were adjusted to reproduce the same radial centrifugal stress variation in the blade.

The entire three-dimensional blade was redesigned with 24 optimization design variables at five spanwise sections (Table 1). The two internal ribs of the actual design were initially vertical. During the optimization, five two dimensional design sections controlled the rib positions. The die pull angles of both ribs were also part of the design variable set, but fixed radially to account for castability. The internal coolant walls were enhanced with two sets of ribbed turbulators (TRPs) for each leading and midbody coolant passage. The strips of boundary-layer turbulators were placed on the suction and pressure sides along the entire radial span of the two passages up until the first tip turn. The heights, streamwise pitches, and skew angles of each pair of TRPs were controlled by the optimization design variable set. The trailing-edge coolant passage was cooled

Table 1 Design variables of the F100 second high-pressure turbine blade optimization for increased cooling effectiveness

Design variable	Number in set	Minimum	Maximum
Die pull angle θ_S	1 per rib (2)	−10 deg	65 deg
Rib position x_{rp}	5 per rib (10)	Variable	Variable
Turbulator height ε	2 per cavity (4)	$0.04 \times H$	$0.25 \times H$
Turbulator pitch p	2 per cavity (4)	$5 \times \varepsilon$	$70 \times \varepsilon$
Turbulator skew α	2 per cavity (4)	0 deg	90 deg
Total number	24	——	——

with pedestals that were shaped and positioned for cooling purposes, as well as to provide increased stiffness against vibration. In this optimization, the relative dimensions of the pedestals were fixed.

The minimum and maximum bounds on the optimization design variables are also given in Table 1. The turbulator heights and pitches were limited by the range of validity of their empirical correlations.[25,28] For example, the bounds on the turbulator heights were limited by the coolant passage height H between the suction and pressure sides, and the turbulator pitches were limited by a factor of turbulator heights ε. The bounds of the rib positions were set to produce a geometrically feasible design. To set the manufacturing constraints, the coolant passage walls were filleted, draft was included in the ribs, and the die pull angles θ_S were constant along the span.

The BEM temperature field was used in conjunction with the cooling effectiveness to develop the objective function F [Eq. (3)]. The fully coupled aerothermofluid solution procedure was used to develop this function for each design perturbation, whereas the constrained evolutionary algorithm maximized the cooling effectiveness objective function.[3,29] In serial processing mode, the entire optimization process utilized a full week of computing time on a Sun Ultra-60 workstation. About 630 objective function analyses were required, resulting in approximately 1400 simulations of the temperature field using the BEM.

The optimization starting point, which was the production version of the F100 second turbine blade design, had an integrated average cooling effectiveness of 25.85%. The cooling effectiveness of the three-dimensional optimized design was 30.8%. Note that this cooling effectiveness was surface-area averaged over the entire external surface. There was little improvement in the wall temperature at the tip of the blade because the tip and turn surfaces were assumed to be adiabatic. The section-averaged cooling effectiveness of the root, quarter-root, and midspan sections demonstrated a more significant improvement. Figures 10a and 10b show the external wall temperature variation predicted by the coupled aerothermofluid analysis at the midspan and quarter-root span. Note that the temperatures have been normalized to protect company proprietary information.

The section-averaged wall temperatures were more than 50°F lower in the optimized design. This was accomplished in several ways. Notice that the optimization algorithm reduced the internal ribbed turbulator heights near the root of the leading-edge coolant passage. Figure 11 clearly demonstrates this optimization trend. Figure 11 shows the history of the turbulator height design variables during the optimization run. Remember that the design variable set included four turbulator heights ε, two in each coolant passage and, within each coolant passage, one a constant height from the root to about the two-thirds span and the other from two-thirds span to the tip. The former are shown as filled symbols and the latter are shown as open symbols. The turbulator heights in the leading-edge coolant passage (cavity in Fig. 11) are circles and the midbody coolant passage (cavity in Fig. 11) are squares. The internal turbulator heights of the actual F100 second blade design were relatively tall, but the optimization algorithm reduced them to their smallest allowable value as set by the lower design variable bound. That bound was set by the range of validity of the correlation in the internal coolant flow model. Notice that the optimization algorithm reduced the leading-edge root values of ε to its lower bound and stayed on that lower bound, indicating that the optimizer was trying to remove that internal heat transfer enhancement. The reason for this is now clear. By the removal of the leading-edge root turbulators, less heat will be absorbed by the blade so that the coolant air would be cooler downstream. Unfortunately, the reduced internal heat transfer coefficients at the leading-edge root had a penalizing effect. The stagnation point at the leading edge of the blade was hotter in the optimized configuration, and this was more pronounced at the blade root. The optimization objective was a globally integrated function, and so the localized heating at the leading edge had only a small effect. This is interpreted as a problem with the integrated average cooling effectiveness objective function [Eq. (3)]. It would be more appropriate to weight more heavily the localized hot spots, particularly at the leading and trailing edges, to penalize optimization trends that cause them.
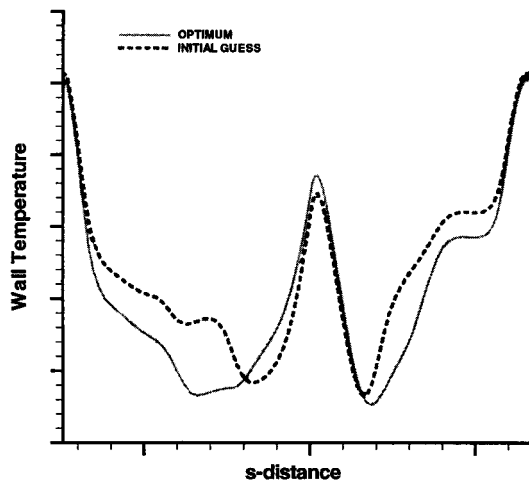
Fig. 10a Comparison of external wall temperature predicted by the BEM at the midspan of the second HPT blade of the F100 engine; optimization starting point is shown as a dashed line and optimized design is shown as the solid line.
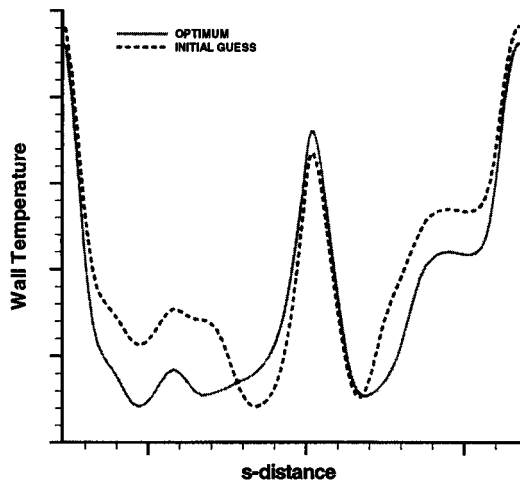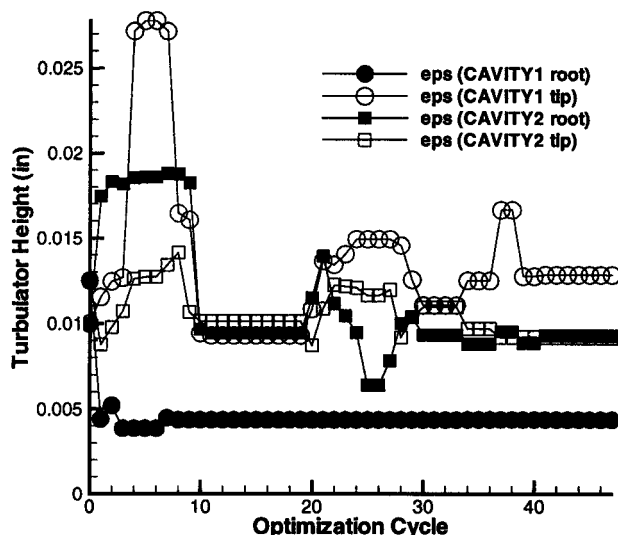

Fig. 10b Comparison of external wall temperature predicted by BEM at the quarter-root span of the second HPT blade of the F100 engine; optimization starting point is shown as a dashed line and optimized design is shown as the solid line.

Fig. 11 History of turbulator height design variables during cooling effectiveness optimization of F100 second turbine blade.
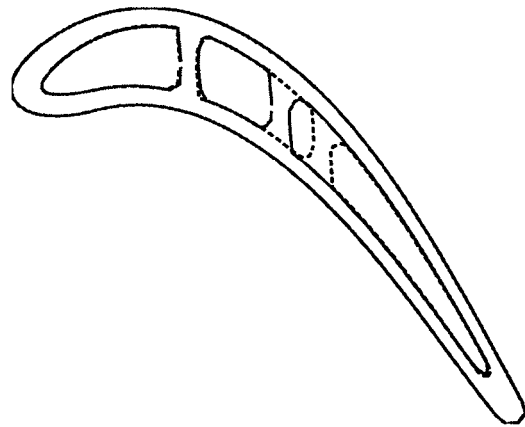
Fig. 12 Comparison between the initial design (---) and final optimized design (——) is shown at the six design sections of Pratt and Whitney F100 second turbine blade.

The cross sections at one two-dimensional design section are shown in Fig. 12. The initial (production) design of the Pratt and Whitney F100 second turbine blade is shown as dashed lines. The optimized geometries are shown as solid lines. The optimization algorithm attempted to move the rib positions to do two things. First, the leading-edge rib near the blade root was moved aft to produce a larger cross-sectional area in the leading-edge coolant passage. This would allow for lower coolant Mach numbers at the trailing-edge root. That effect was sought out because lower coolant speeds were correlated to lower heat transfer coefficients on the coolant passage walls, which would cause the coolant to absorb less heat. Second, the optimization algorithm moved the middle rib at the tip toward the leading edge to produce the opposite effect. The cross section clearly demonstrates a smaller cross-sectional area just after the first turn. In the fluid elements of the middle coolant passage near the tip, the internal flow Mach numbers increased from about 0.11 to 0.15. Combined with the increased turbulator height, the corresponding internal heat transfer coefficients were increased by about 45%. The optimization algorithm was favoring higher heat transfer coefficients in areas of the blade that were hotter, but it did this by sacrificing leading-edge cooling.

The net effects of all of these design modifications were that the cooling effectiveness increased by 5%, whereas the coolant supply pressure remained the same, and the coolant mass flow rate was increased by only 0.5%. This increase is marginal when compared to the core engine flow rate, whereas the reduction in metal temperature by 50°F is substantial because it yields a doubling in the creep life of the blade at the F100 engine operating conditions. The optimization algorithm found a design that achieved a 5% improvement in cooling effectiveness with only $\frac{1}{10}$th more cooling air than what would normally be used to achieve it. For example, if the design had remained fixed by assuming that the objective function $F(V)$ in Eq. (3b) stays the same, the same increase in the cooling effectiveness would require a 5% increase in the coolant flow rate.

XV. Conclusions

Given that the optimization starting point was the actual production version of the turbine blade that probably went through several manual design cycles, and considering that the optimization algorithm found an improved design that had more than a 50°F lower section-averaged metal temperature, this demonstration was successful at achieving the goals set to it, and the multidisciplinary design and optimization methodology can be considered to be valid. This improvement in metal temperature would correlate to a factor of two improvements in creep life.

Further optimization of this turbine blade is also possible. The pedestal diameters and relative spacings could be included in the design variable set in an attempt to reduce the wall temperatures at the trailing edge. For a more accurate prediction of the temperature field in the trailing passage, the pedestals would need to be included

in the thermal model (rather than just as a thermal boundary condition to a smooth coolant passage wall). There are also other possibilities. The external turbine blade shape could be modified in an effort to make the external aerothermodynamics reduce the amount of heat absorbed by the blade. Each new design of the external airfoil would require a fully conjugate viscous three-dimensional steady-state CFD analysis of the hot gas flowfield and the temperature field inside the blade.[28] This CFD solution would then be used to predict new external heat transfer coefficients, as well as to provide an aerodynamic constraint function so that the efficiency and work of the turbine row could be fixed.[29]

Acknowledgments

References

[1]Lakshminarayana, B., *Fluid Dynamics and Heat Transfer of Turbomachinery*, Wiley, New York, 1996, pp. 597–721.

[2]Martin, T. J., *Computer-Automated Multi-Disciplinary Analysis and Design Optimization of Internally Cooled Turbine Blades*, Ph.D. Dissertation, Dept. of Aerospace Engineering, Pennsylvania State Univ., University Park, PA, May 2001.

[3]Martin, T. J., and Dulikravich, G. S., "Aero-Thermo-Elastic Concurrent Design Optimization of Internally Cooled Turbine Blades," *Coupled Field Problems, Series on Advances in Boundary Elements*, edited by A. J. Kassab and M. H. Aliabadi, WIT Press, Boston, 2001, pp. 137–184.

[4]Martin, T. J., and Dulikravich, G. S., "Aero-Thermal Analysis and Optimization of Internally Cooled Turbine Blades," *XIII International Symposium on Air-breathing Engines*, edited by F. Billig, Chattanooga, TN, ISABE 97-7165, Vol. 2, 1997, pp. 1232–1250.

[5]Martin, T. J., Dulikravich, G. S., Han, Z.-X., and Dennis, B. H., "Minimization of Coolant Mass Flow Rate in Internally Cooled Gas Turbine Blades," American Society of Mechanical Engineers, ASME Paper 99-GT-146, June 1999.

[6]Dulikravich, G. S., Martin, T. J., Dennis, B. H., and Foster, N. F., "Multidisciplinary Hybrid Constrained GA Optimization," *EUROGEN'99-Evolutionary Algorithms in Engineering and Computer Science: Recent Advances and Industrial Applications*, edited by K. Miettinen, M. M. Makela, P. Neittaanmaki, and J. Periaux, Wiley, Chichester, UK, 1999, pp. 231–260.

[7]Larson, F. R., and Miller, J., "A Time Temperature Relationship for Rupture and Creep Stresses," *ASME Journal*, Vol. 74, 1952, p. 765.

[8]Menon, M. N., "A Model for Primary, Secondary and Tertiary Creep Rates," *Proceedings of the 5th International Conference on Creep of Materials*, Lake Bueua Vista, FL, May 1992.

[9]Chima, R. V., "Explicit Multigrid Algorithm for Quasi-Three-Dimensional Viscous Flows in Turbomachinery," *Journal of Propulsion and Power*, Vol. 3, No. 5, 1987, p. 397.

[10]Chima, R. V., "A k–ω Turbulence Model for Quasi-Three-Dimensional Turbomachinery Flows," AIAA Paper 96-0248, Jan. 1995.

[11]Giel, P. W., Thurman, D. R., Van Fossen, G. J., Hippensteele, S. A., and Boyle, R. J., "Endwall Heat Transfer Measurements in a Transonic Turbine Cascade," *Journal of Turbomachinery*, Vol. 120, April 1998, pp. 305–313.

[12]Brebbia, C. A., *The Boundary Element Method for Engineers*, Wiley, New York, 1978.

[13]Brillert, D., Reichert, A. W., and Simon, H., "Calculation of Flow Losses in Rotating Passages of Gas Turbine Cooling Systems," American Society of Mechanical Engineers, ASME Paper 99-GT-251, June 1999.

[14]White, F. M., *Fluid Mechanics*, 3rd ed., McGraw–Hill, New York, 1994, pp. 342–348.

[15]Kawaike, K., Shunichi, A., and Sasada, T., "Integrated CAE System for Cooled Turbine Blade Design and Verification Tests of Analytical Codes," *Proceedings of the International Symposium on Heat Transfer in Turbomachinery*, edited by R. J. Goldstein, D. E. Metzger, and A. I. Leontiev, Athens, Greece, Begell House, New York, 1992.

[16]Gritsch, M., Schulz, A., and Wittig, S., "Discharge Coefficient Measurements of Film-Cooling Holes with Expanded Jets," American Society of Mechanical Engineers, ASME Paper 97-GT-165, June 1997.

[17]Press, W. H., Teukolsky, S. A., Vetterling, W. T., and Flannery, B. P., *Numerical Recipes in FORTRAN, The Art of Scientific Computing*, 2nd ed., Cambridge Univ. Press, Cambridge, England, U.K., 1986.

[18]White, F. M., *Viscous Fluid Flow*, McGraw–Hill, New York, 1974, Chap. 6, pp. 454–575.

[19]Webb, R. L., *Principles of Enhanced Heat Transfer*, Wiley, New York, 1998, pp. 229–242.

[20]Schlichting, H., *Boundary Layer Theory*, 7th Edition, translated by J. Kestin, McGraw–Hill, New York, 1979.

[21]Dipprey, D. F., and Sabersky, R. H., "Heat and Momentum Transfer in Smooth and Rough Tubes at Various Prandtl Number," *International Journal of Heat and Mass Transfer*, Vol. 6, 1963, pp. 329–353.

[22]Han, J.-C., and Park, J. S., "Developing Heat Transfer in Rectangular Channels with Rib Turbulators," *International Journal of Heat Mass Transfer*, Vol. 31, No. 1, 1988, pp. 183–195.

[23]White, F. M., *Heat and Mass Transfer*, Addison Wesley Longman Reading, MA, 1988, Chap. 5, pp. 285–362.

[24]Holman, J. P., *Heat Transfer*, 5th ed., McGraw–Hill, New York, 1981.

[25]Mochizuki, S., Takamura, J., Yamawaki, S., and Yang, W. J., "Heat Transfer in Serpentine Flow Passages with Rotation," *Journal of Turbomachinery*, Vol. 116, 1994, pp. 133–140.

[26]Crawford, M. E., and Kayes, W. M., "STAN5—Program for Numerical Computation of Two-Dimensional Internal and External Boundary Layer Flows," NASA CR-2742, 1976.

[27]Han, Z.-X., Dennis, B. H., and Dulikravich, G. S., "Simultaneous Prediction of External Flow-Field and Temperature in Internally Cooled 3-D Turbine Blade Material," *International Journal of Turbo and Jet Engines*, Vol. 18, No. 1, 2001, pp. 47–58.

[28]Han, J.-C., Zhang, Y. M., and Lee, C. P., "Influence of Surface Heating Condition on Local Heat Transfer in a Rotating Square Channel with Smooth Walls and Radial Outward Flow," *Journal of Turbomachinery*, Vol. 116, 1994, pp. 149–158.

[29]Dennis, B. H., Dulikravich, G. S., and Han, Z.-X., "Constrained Optimization of Turbomachinery Airfoil Shapes Using a Navier–Stokes Solver and a Genetic/SQP Algorithm," *Journal of Propulsion and Power*, Vol. 17, No. 5, 2001, pp. 1123–1128.